Available online at www.sciencedirect.com

ScienceDirect

Geochimica et Cosmochimica Acta 265 (2019) 148–162

Geochimica et Cosmochimica Acta

www.elsevier.com/locate/gca

Pyrite $\delta^{34}S$ and $\Delta^{33}S$ constraints on sulfur cycling at sublacustrine hydrothermal vents in Yellowstone Lake, Wyoming, USA

Andrew P.G. Fowler [a,*,1], Qiu-li Liu [b,c], Yongshu Huang [b,c], Chunyang Tan [a], Michael W.R. Volk [a,d], W.C. Pat Shanks III [e], William Seyfried Jr. [a]

[a] Department of Earth Sciences, University of Minnesota, Minneapolis, MN 55455, USA
[b] State Key Laboratory of Lithospheric Evolution, Institute of Geology and Geophysics, Chinese Academy of Sciences, Beijing 100029, China
[c] College of Earth Science, University of Chinese Academy of Sciences, Beijing 100049, China
[d] Department of Earth and Planetary Sciences, Harvard University, Cambridge, MA 02138, USA
[e] U.S. Geological Survey, Denver Federal Center, MS 973, Denver, CO 80225-0046, USA

Received 20 April 2019; accepted in revised form 2 September 2019; available online 10 September 2019

Abstract

Sulfur isotope values ($\delta^{34}S$ and $\Delta^{33}S$) of pyrite in sediment from steam-heated hydrothermal vents on the floor of Yellowstone Lake (WY) were measured using secondary ionization mass spectrometry (SIMS). The high resolution of the SIMS data place important constraints on sulfur cycling processes at/near the vent fluid-lake water interface. Pyrite with a distinct mantle-basalt ($\delta^{34}S = 0‰$) isotope composition ($\delta^{34}S = +0.5$ to $+3.1‰$) replaces pyrrhotite during incipient stages of alteration at moderately high temperature. Disseminated cubic pyrite ($\delta^{34}S = +2.0$ to $+5.3‰$) occurs in zones where more extensive oxidation is likely. Framboidal pyrite with $\delta^{34}S$ values ranging from –5.2 to +4.1‰ and $\Delta^{33}S$ up to +0.30‰ suggest formation from low-temperature microbial sulfate reduction in sediments near but not directly in the vent fluid up-flow zone. The co-occurrence of pyrite with S isotope values characteristic of distinct formation processes, coupled with notable intracrystal S isotope variations, suggests the venting locus is dynamic in time and space.

Keywords: Yellowstone Lake; SIMS; Sulfur isotopes; Pyrite; Pyrrhotite; Sublacustrine; Hydrothermal dynamics

1. INTRODUCTION

Recent efforts to understand how the Yellowstone Lake hydrothermal system responds to environmental perturbations (Sohn et al., 2017) have led to careful study involving, *in situ* physical and chemical measurements, and sampling of several non-constructional hydrothermal vents in the deepest (100 to 125 m; the Deep Hole) region of the lake (Fig. 1A). Chemical and temperature sensors inserted >10 cm into vent openings recorded a maximum fluid temperature of 174 °C, making these the hottest sublacustrine hydrothermal vents yet identified (Tan et al., 2017; Fowler et al., 2019). Moreover, *in situ* chemical data indicate that the vent fluids are notably reducing (Eh of −0.2 to −0.3 volts) with pH values of 4.25–4.5 (Tan et al., 2017). The chemistry and stable isotope values of the Deep Hole sublacustrine hydrothermal fluids indicate that they are CO_2-, H_2S-, and H_2-bearing steam condensate that has mixed with oxygenated, neutral pH (~7.5), cold (10–15 °C) lake water (Fowler et al., 2019). The vents are hosted

* Corresponding author.
E-mail address: andrew.fowler@ehs-support.com (A.P.G. Fowler).
[1] Presently Senior Geologist at EHS Support.

https://doi.org/10.1016/j.gca.2019.09.004
0016-7037/

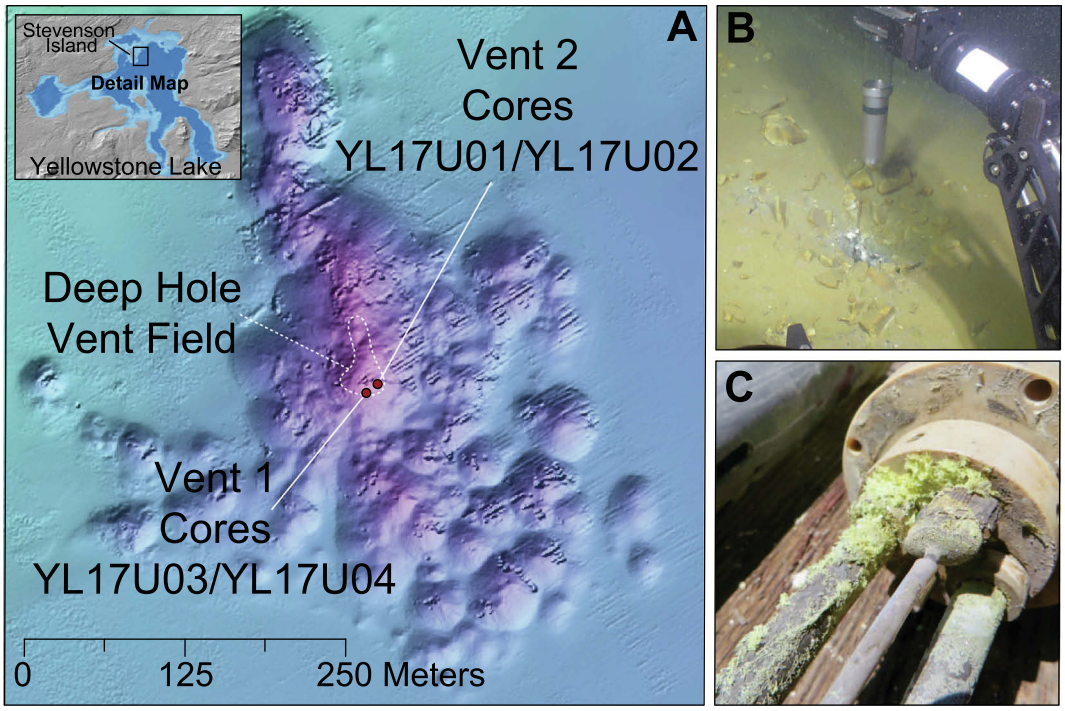

Fig. 1. (A): Location of the Deep Hole hydrothermal field east of Stevenson Island, Yellowstone Lake. The extent of the known field is given by a dashed line, sediment coring locations are indicated with circles. Map modified from (Sohn et al., 2017) and (Fowler et al., 2019). (B): ROV Yogi preparing to collect sediment core YL17U03 from Vent 1. (C): Native sulfur crystals formed on an Eh-pH sensor that was deployed in a core hole for one year.

in extensively altered sediments that are composed largely of pyrite-bearing kaolinite, with boehmite and trace pyrrhotite. Four push cores up to 19 cm long were recovered, with two from within active vents and two offset about 1 meter from the vents, using a remotely operated submersible vehicle (ROV) (Fig. 1B). Moreover, an integrated chemical and temperature sensor system was deployed for a year starting in August 2017 in an active vent; recovery of this instrument package in August 2018 revealed a coating of native sulfur crystals and pyrite, confirming localized sulfur-saturated conditions (Fig. 1C). Variations in the sulfur isotope composition of pyrite in vent sediments at the locus of mixing between cold, neutral pH and oxidized lake water and hot, acidic and reduced steam condensate provide a means to examine evolving conditions at a sublacustrine hydrothermal vent. The motivation of the present study is to examine relations between active hydrothermal venting in the Deep Hole and textural and spatial variations in sulfur-bearing minerals and in the sulfur isotope composition of pyrite to better understand sulfur cycling in this unique hydrothermal system.

2. IRON SULFIDE REACTION MECHANISMS

Pyrite is one of the most abundant sulfide minerals on Earth. Its widespread occurrence attests to the diverse range of formation pathways that have been documented from field and experimental studies (Berner, 1970; Luther, 1991; Sweeney and Kaplan, 1973; Rickard, 1975; Rickard, 1997; Schieber, 2002; Butler et al., 2004). At relatively high temperatures, uncatalyzed sulfate reduction at intermediate redox conditions can provide a nascent source of dissolved H_2S, especially at moderately low pH conditions where favorable reaction kinetics prevail (Ohmoto and Lasaga, 1982; Woodruff and Shanks, 1988). Pyrite from marine hydrothermal settings, including seafloor chimney deposits and in subsurface upflow zones, illustrate this best as indicated by distinctive sulfur isotope compositions (Shanks et al., 1981; Shanks and Seyfried, 1987; Shanks, 2001).

Pyrite formation at relatively low temperatures (<150 °C) generally is dependent on the availability of catalysts that facilitate electron transfer (Vazquez et al., 1989; Luther et al., 2001; Gartman et al., 2011). Sulfate reduction resulting in pyrite formation under favorable pH and redox conditions is frequently biologically mediated (Jørgensen, 1990; Jørgensen et al., 1990) if conditions are within the temperature limit of life (≤122 °C). Distinctive sulfur isotope fractionations provide useful tools to identify microbial sulfate reduction through careful study of sulfide minerals (Canfield, 2001; Rouxel et al., 2008; Ono et al., 2012). Microbial sulfate reduction can produce substantial $\delta^{34}S$ depletions in the product sulfide of up to 70‰ (Kaplan and Rittenberg, 1964; Canfield and Thamdrup, 1994; Slack et al., 2019), with the extent of fractionation dependent upon a number of factors including ΣSO_4^{2-} and metabolic pathways (Canfield, 2001). Furthermore, microbial sulfate reduction has been shown to produce distinctive mass independent isotope fractionation effects apparent in $\Delta^{33}S$ values that can exceed 0.3‰ as recorded by pyrite (Farquhar et al., 2003; Ono et al., 2006; Ono

Table 1
SIMS analytical results for pyrite $\delta^{34}S$, $\delta^{33}S$, and calculated $\Delta^{33}S$.

Sample	$\delta^{33}S$ VCDT	2SE	$\delta^{34}S$ VCDT	2SE	$\Delta^{33}S$
YL17U01 (2.5 cm) - Cubic pyrite					
YL17U01-2.5 cm-CubPy-1–1	2.0	0.05	3.9	0.05	≤0.1
YL17U01-2.5 cm-CubPy-2–2	2.6	0.04	4.9	0.04	≤0.1
YL17U01-2.5 cm-CubPy-2–3	2.8	0.05	5.2	0.05	≤0.1
YL17U01-2.5 cm-CubPy-3–5	1.8	0.05	3.5	0.06	≤0.1
YL17U01-2.5 cm-CubPy-4–7	1.9	0.05	3.7	0.02	≤0.1
YL17U01-2.5 cm-CubPy-5–9	2.7	0.04	5.1	0.02	≤0.1
YL17U01-2.5 cm-CubPy-6–10	2.5	0.04	4.7	0.02	≤0.1
YL17U01 (2.5 cm) - Framboidal pyrite					
YL17U01-2.5 cm-FramPy-1–8	−1.0	0.06	−2.2	0.06	≤0.1
YL17U01-2.5 cm-FramPy-2–6	1.9	0.05	3.1	0.04	0.3
YL17U01-2.5 cm-FramPy-3–4	−0.8	0.09	−1.9	0.14	0.2
YL17U01-2.5 cm-FramPy-4–11	2.3	0.04	4.1	0.07	≤0.1
YL17U02 (2 cm) - Framboidal pyrite					
YL17U02-2 cm-FramPy-1–1	0.6	0.04	0.6	0.05	0.3
YL17U02-2 cm-FramPy-1–2	0.2	0.05	−0.2	0.06	0.2
YL17U02-2 cm-FramPy-1–3	−1.9	0.11	−4.0	0.18	0.2
YL17U02-2 cm-FramPy-1–4	−0.4	0.06	−1.2	0.10	0.3
YL17U02-2 cm-FramPy-2–5	0.0	0.05	−0.5	0.06	0.2
YL17U02-2 cm-FramPy-2–6	0.5	0.08	0.6	0.13	0.2
YL17U02-2 cm-FramPy-2–7	0.7	0.08	0.9	0.12	0.2
YL17U02-2 cm-FramPy-2–8	0.7	0.04	0.9	0.03	0.3
YL17U02-2 cm-FramPy-3–13	−0.6	0.06	−1.6	0.06	0.2
YL17U02-2 cm-FramPy-3–14	−1.3	0.08	−3.1	0.10	0.3
YL17U02-2 cm-FramPy-3–15	−1.2	0.05	−2.7	0.03	0.2
YL17U02-2 cm-FramPy-4–16	−0.4	0.07	−1.2	0.05	0.2
YL17U02-2 cm-FramPy-4–17	0.3	0.06	0.1	0.04	0.2
YL17U02-2 cm-FramPy-4–18	0.2	0.07	0.2	0.03	≤0.1
YL17U02-2 cm-FramPy-4–19	−2.6	0.10	−5.2	0.14	≤0.1
YL17U02-2 cm-FramPy-4–20	−1.8	0.09	−3.7	0.14	≤0.1
YL17U02-2 cm-FramPy-5–27	0.2	0.05	0.1	0.04	0.2
YL17U02-2 cm-FramPy-5–29	−1.4	0.05	−3.0	0.05	≤0.1
YL17U02 (2 cm) - Pseudo framboidal pyrite					
YL17U02-2 cm-PframPy-1–9	2.4	0.04	4.3	0.03	≤0.1
YL17U02-2 cm-PframPy-1–10	2.2	0.05	4.0	0.05	0.2
YL17U02-2 cm-PframPy-1–11	2.1	0.04	3.8	0.05	0.2
YL17U02-2 cm-PframPy-1–12	1.9	0.05	3.4	0.08	0.2
YL17U02-2 cm-PframPy-1–21	2.2	0.04	4.0	0.03	≤0.1
YL17U02-2 cm-PframPy-1–22	2.2	0.05	4.0	0.04	≤0.1
YL17U02-2 cm-PframPy-1–23	2.1	0.06	3.8	0.05	≤0.1
YL17U02-2 cm-PframPy-1–24	2.0	0.05	3.6	0.04	0.2
YL17U02-2 cm-PframPy-1–25	2.1	0.06	3.9	0.04	≤0.1
YL17U02-2 cm-PframPy-1–26	2.1	0.04	3.8	0.03	≤0.1
YL17U02 (16 cm) - Cubic pyrite					
YL17U02-16 cm-LCubPy-1–1	1.6	0.05	3.0	0.05	≤0.1
YL17U02-16 cm-LCubPy-1–2	1.6	0.06	3.0	0.08	≤0.1
YL17U02-16 cm-LCubPy-1–3	1.6	0.05	2.9	0.07	≤0.1
YL17U02-16 cm-LCubPy-1–4	1.5	0.03	2.7	0.03	≤0.1
YL17U02-16 cm-LCubPy-1–5	2.0	0.04	3.8	0.06	≤0.1
YL17U02-16 cm-LCubPy-1–6	2.3	0.04	4.4	0.04	≤0.1
YL17U02-16 cm-CubPy-2–7	2.3	0.05	4.4	0.04	≤0.1
YL17U02-16 cm-CubPy-3–8	2.3	0.05	4.4	0.06	≤0.1
YL17U02-16 cm-CubPy-4–9	2.5	0.06	4.7	0.06	≤0.1
YL17U02-16 cm-CubPy-5–10	2.6	0.04	5.0	0.04	≤0.1
YL17U02-16 cm-CubPy-6–11	1.9	0.06	3.5	0.02	≤0.1
YL17U02-16 cm-CubPy-6–12	2.4	0.05	4.4	0.02	≤0.1
YL17U02-16 cm-CubPy-6–13	2.0	0.06	3.8	0.02	≤0.1
YL17U02-16 cm-CubPy-6–14	2.2	0.04	4.1	0.03	≤0.1
YL17U02-16 cm-CubPy-7–15	1.3	0.05	2.3	0.03	≤0.1

(*continued on next page*)

Table 1 (*continued*)

Sample	$\delta^{33}S$ VCDT	2SE	$\delta^{34}S$ VCDT	2SE	$\Delta^{33}S$
YL17U02-16 cm-CubPy-8–16	2.1	0.05	3.9	0.02	≤0.1
YL17U02-16 cm-CubPy-9–17	1.8	0.07	3.2	0.08	≤0.1
YL17U02-16 cm-CubPy-10–18	2.2	0.05	4.1	0.02	≤0.1
YL17U02-16 cm-CubPy-11–19	2.4	0.04	4.6	0.02	≤0.1
YL17U02-16 cm-CubPy-12–20	1.8	0.06	3.3	0.04	≤0.1
YL17U02-16 cm-CubPy-13–21	2.2	0.04	4.1	0.04	≤0.1
YL17U02 (6 cm) - Sulfide Vein					
YL17U02-6 cm-VeinPy-1–1	2.3	0.03	4.4	0.04	≤0.1
YL17U02-6 cm-VeinPy-1–2	2.0	0.05	3.9	0.05	≤0.1
YL17U02-6 cm-VeinPy-1–3	2.0	0.04	3.9	0.05	≤0.1
YL17U02-6 cm-VeinPy-1–4	2.0	0.05	3.9	0.05	≤0.1
YL17U02-6 cm-VeinPy-1–5	2.0	0.04	4.0	0.03	≤0.1
YL17U02-6 cm-VeinPy-2–6	1.9	0.04	3.5	0.06	≤0.1
YL17U02-6 cm-VeinPy-2–7	2.2	0.03	4.0	0.03	≤0.1
YL17U02-6 cm-VeinPy-2–8	2.1	0.05	4.1	0.02	≤0.1
YL17U02-6 cm-VeinPy-2–9	2.1	0.05	4.0	0.03	≤0.1
YL17U02-6 cm-VeinPy-3–10	1.8	0.05	3.5	0.02	≤0.1
YL17U02-6 cm-VeinPy-3–11	1.9	0.07	3.7	0.03	≤0.1
YL17U02-6 cm-VeinPy-3–12	2.1	0.05	4.0	0.03	≤0.1
YL17U02-6 cm-VeinPy-3–13	2.2	0.04	4.0	0.03	≤0.1
YL17U02-6 cm-VeinPy-3–14	2.0	0.04	3.8	0.02	≤0.1
YL17U02-6 cm-VeinPy-4–15	2.1	0.05	4.1	0.03	≤0.1
YL17U02-6 cm-VeinPy-4–16	2.3	0.05	4.3	0.04	≤0.1
YL17U02-6 cm-VeinPy-4–17	2.5	0.05	4.6	0.03	≤0.1
YL17U02-6 cm-VeinPy-4–18	1.9	0.05	3.7	0.04	≤0.1
YL17U02-6 cm-VeinPy-4–19	2.3	0.04	4.4	0.03	≤0.1
YL17U02-6 cm-VeinPy-5–20	1.7	0.06	3.2	0.06	≤0.1
YL17U02-6 cm-VeinPy-5–21	1.9	0.05	3.6	0.02	≤0.1
YL17U02-6 cm-VeinPy-5–22	1.9	0.05	3.8	0.03	≤0.1
YL17U02-6 cm-VeinPy-5–23	2.0	0.04	3.7	0.02	≤0.1
YL17U03 (10 cm) - Cubic Pyrite					
YL17U03-10 cm-CubPy-1–3	2.4	0.06	4.4	0.06	≤0.1
YL17U03-10 cm-CubPy-1–4	2.3	0.06	4.4	0.06	≤0.1
YL17U03-10 cm-CubPy-2–8	2.2	0.05	4.1	0.05	≤0.1
YL17U03-10 cm-CubPy-2–9	2.3	0.04	4.3	0.04	≤0.1
YL17U03-10 cm-CubPy-3–10	1.7	0.05	3.3	0.06	≤0.1
YL17U03-10 cm-CubPy-3–11	1.7	0.04	3.2	0.05	≤0.1
YL17U03-10 cm-CubPy-3–12	1.8	0.04	3.5	0.03	≤0.1
YL17U03-10 cm-CubPy-4–13	1.8	0.04	3.4	0.03	≤0.1
YL17U03-10 cm-CubPy-4–14	1.2	0.06	2.2	0.03	≤0.1
YL17U03-10 cm-CubPy-5–15	2.0	0.05	3.9	0.02	≤0.1
YL17U03-10 cm-CubPy-5–16	1.1	0.05	2.0	0.04	≤0.1
YL17U03-10 cm-CubPy-5–17	1.1	0.05	2.3	0.03	≤0.1
YL17U03-10 cm-CubPy-6–18	2.0	0.04	3.7	0.03	≤0.1
YL17U03-10 cm-CubPy-6–19	2.5	0.05	4.9	0.03	≤0.1
YL17U03-10 cm-CubPy-7–20	2.8	0.04	5.2	0.03	≤0.1
YL17U03-10 cm-CubPy-7–21	2.4	0.06	4.5	0.04	≤0.1
YL17U03-10 cm-CubPy-7–22	2.8	0.05	5.3	0.03	≤0.1
YL17U03-10 cm-CubPy-7–23	2.2	0.05	4.2	0.04	≤0.1
YL17U03-10 cm-CubPy-8–24	1.7	0.05	3.4	0.02	≤0.1
YL17U03-10 cm-CubPy-8–25	1.7	0.05	3.3	0.03	≤0.1
YL17U03-10 cm-CubPy-8–26	1.9	0.04	3.6	0.01	≤0.1
YL17U04 (2 cm) - Pyrite after pyrrhotite					
YL17U04-2 cm-PoPy-1–4	1.2	0.05	2.3	0.03	≤0.1
YL17U04-2 cm-PoPy-1–5	1.7	0.05	3.1	0.03	≤0.1
YL17U04-2 cm-PoPy-1–6	1.1	0.06	2.0	0.08	≤0.1
YL17U04-2 cm-PoPy-2–7	0.6	0.06	1.0	0.04	≤0.1
YL17U04-2 cm-PoPy-2–8	0.3	0.06	0.6	0.06	≤0.1
YL17U04-2 cm-PoPy-2–9	0.3	0.06	0.5	0.09	≤0.1

Table 1 (*continued*)

Sample	$\delta^{33}S$ VCDT	2SE	$\delta^{34}S$ VCDT	2SE	$\Delta^{33}S$
YL17U04 (2 cm) - Cubic pyrite					
YL17U04-2 cm-CubPy-1–1	1.7	0.05	3.3	0.06	≤0.1
YL17U04-2 cm-CubPy-2–1	2.7	0.04	5.1	0.03	≤0.1
YL17U04-2 cm-CubPy-2–17	2.2	0.05	4.0	0.03	≤0.1
YL17U04-2 cm-CubPy-3–18	2.3	0.04	4.4	0.02	≤0.1
YL17U04-2 cm-CubPy-4–19	2.0	0.05	3.7	0.03	≤0.1
YL17U04-2 cm-CubPy-5–2	2.0	0.04	3.9	0.04	≤0.1
YL17U04-2 cm-CubPy-6–3	2.4	0.03	4.5	0.04	≤0.1
YL17U04-2 cm-CubPy-7–4	1.9	0.04	3.7	0.05	≤0.1
YL17U04-2 cm-CubPy-7–5	2.0	0.04	3.9	0.04	≤0.1
YL17U04-2 cm-CubPy-8–6	2.4	0.05	4.4	0.05	≤0.1
YL17U04-2 cm-CubPy-8–7	2.6	0.06	4.7	0.04	≤0.1
YL17U04-2 cm-CubPy-9–8	2.1	0.05	4.0	0.05	≤0.1
YL17U04-2 cm-CubPy-9–9	2.4	0.05	4.5	0.04	≤0.1
YL17U04-2 cm-CubPy-9–20	2.6	0.05	4.8	0.03	≤0.1
YL17U04-2 cm-CubPy-10–10	1.5	0.06	2.8	0.09	≤0.1
YL17U04-2 cm-CubPy-10–11	2.1	0.05	4.0	0.04	≤0.1
YL17U04-2 cm-CubPy-10–12	2.2	0.05	4.2	0.07	≤0.1
YL17U04-2 cm-CubPy-10–21	1.8	0.05	3.4	0.03	≤0.1
YL17U04-2 cm-CubPy-11–13	2.4	0.04	4.5	0.03	≤0.1
YL17U04-2 cm-CubPy-11–22	2.2	0.04	4.1	0.02	≤0.1
YL17U04-2 cm-CubPy-12–14	2.4	0.05	4.5	0.05	≤0.1
YL17U04-2 cm-CubPy-12–15	2.2	0.04	4.2	0.06	≤0.1
YL17U04-2 cm-CubPy-12–23	2.4	0.04	4.5	0.02	≤0.1
YL17U04-2 cm-CubPy-13–16	2.4	0.04	4.6	0.04	≤0.1

et al., 2007; Rouxel et al., 2008; Ono et al., 2012). Indeed, sulfur metabolizing organisms have been identified at vents in Yellowstone Lake (Yang et al., 2011; Inskeep et al., 2015; Kan et al., 2016), suggesting this is a viable pyrite formation mechanism in the study area.

The highest temperature observed from in-situ measurements of hydrothermal fluid and coexisting sediment samples from the Deep Hole of Yellowstone Lake (174 °C) exceeds the threshold for microbial processes, yet this temperature is below that for direct (chemically uncatalyzed) sulfate reduction for the prevailing chemical conditions. For these conditions, direct nucleation of pyrite is unfavorable and requires sulfidation of an $FeS_{(aq)}$ intermediate (Rickard, 1975; Luther, 1991; Schoonen and Barnes, 1991a; Rickard, 1995; Rickard, 1997). Sulfidation of $FeS_{(aq)}$ to form pyrite may occur following two verified mechanisms: addition of $H_2S_{(aq)}$ "the H_2S pathway" (Eq. (1)), or by addition of more oxidized polysulfide ($S_{n(aq)}^{2-}$) sulfur "the polysulfide pathway" (Eq. (2)) (Berner, 1983; Luther, 1991; Schoonen and Barnes, 1991a; Rickard, 1997; Rickard and Luther, 2007).

$$FeS_{(aq)} + H_2S_{(aq)} \rightarrow FeS_{2(s)} + H_{2(aq)} \quad (1)$$

$$FeS_{(aq)} + S_{n(aq)}^{2-} \rightarrow FeS_{2(s)} + S_{n-1(aq)}^{2-} \quad (2)$$

Sulfidation of $FeS_{(aq)}$ by zero valent sulfur (Eq. (3)), thiosulfate (Eq. (4)), and polythionates (Eq. (5)) has also been proposed for pyrite formation between 70 and 300 °C, however, it is thought that the actual reaction mechanism involves intermediate polysulfide species that form during the sulfide oxidation cycle (Berner, 1970; Schoonen and Barnes, 1991a,b; Rickard, 1975; Wilkin and Barnes, 1996; Butler et al., 2004).

$$FeS_{(aq)} + S^0 \rightarrow FeS_{2(s)} \quad (3)$$

$$FeS_{(aq)} + S_2O_{3(aq)}^{2-} \rightarrow FeS_{2(s)} + SO_{3(aq)}^{2-} \quad (4)$$

$$FeS_{(aq)} + S_nO_{6(aq)}^{2-} \rightarrow FeS_{2(s)} + S_{n-1}O_{6(aq)}^{2-} \quad (5)$$

Pyrite formation via solid-state reaction by Fe^{2+} loss from an FeS precursor has also been proposed as a formation mechanism, but has subsequently been shown to be the sum of $FeS_{(s)}$ dissolution and the H_2S pathway (Butler et al., 2004; Rickard and Luther, 2007). Consequently, at moderate temperatures, factors that affect $H_2S_{(aq)}$ concentrations and the metastable oxidation products at hydrothermal mixing interfaces are particularly important for determining abiotic pyrite formation mechanisms. Furthermore, minor S isotope fractionation effects resulting from abiotic sulfide oxidation (Amrani et al., 2006; Kamyshny et al., 2014) are reflected in the $\delta^{34}S$ of resulting pyrite (Butler et al., 2004).

The distinctive sulfur isotope fractionations from microbial and abiotic processes during pyrite formation at oxic/anoxic interfaces have been proposed as a tool to distinguish evolving chemical conditions and paleoenvironmental conditions (Canfield et al., 1998; Butler et al., 2004; Ono et al., 2007). In the present study, we utilize secondary ionization mass spectrometry (SIMS) analyses of pyrite $\delta^{34}S$ and $\Delta^{33}S$ values to assess the roles of abiotic sulfide oxidation and microbial sulfate reduction at steam-heated sublacustrine vents in Yellowstone Lake. SIMS can provide high spatial resolution (~10–50 μm) analyses for sulfur isotopes (McKibben and Riciputi, 1997), therefore, the technique is useful for examining intragrain $\delta^{34}S$ variations and variations amongst individual pyrite crystals that occur in the

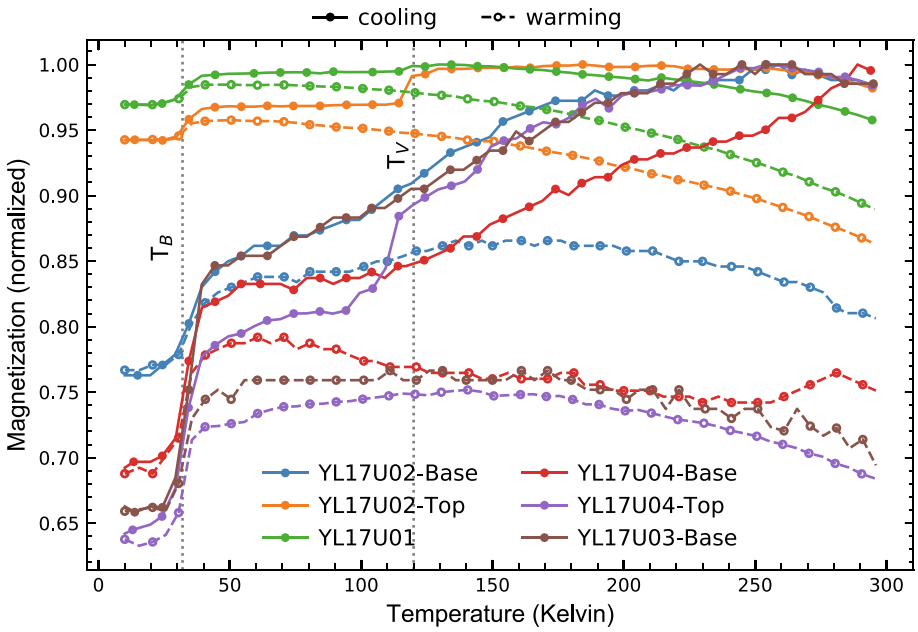

Fig. 2. Room temperature saturating isothermal remnant magnetization (RTSIRM) as a function of temperature, normalized to the room temperature value. All samples show a drop in magnetization at ≈30 K that is typical for the Besnus transition (T_B) of monoclinic pyrrhotite. YL17U02 (Top) and YL17U04 (Top) also show signs of the magnetite Verwey transition (T_V) at ≈120 K. The occurrence of metastable pyrrhotite along with pyrite indicates more reducing conditions prevailed for these sediments at some time in the past, and also provides a source of Fe^{2+} that is ultimately incorporated into pyrite.

Deep Hole vent sediments. Moreover, SIMS can typically resolve $\Delta^{33}S$ variations of within about ±0.1‰ (Mojzsis et al., 2003), which can identify mass independent sulfur isotope fractionation associated with biologic sulfate reduction. We report pyrite with sulfur isotope characteristics that reflect formation by both abiotic H_2S oxidation and microbial sulfate reduction.

3. MATERIALS AND METHODS

3.1. Sample collection and processing

Four, 5 to 19 cm long sediment push cores were obtained from active hydrothermal vents offshore of Stevenson Island in Yellowstone Lake at a water depth of 115 m in August 2017. The cores were recovered using the remotely operated vehicle (ROV) "Yogi" and support vessel R/V Annie that are owned and operated by the Global Foundation for Ocean Exploration. Two-inch diameter titanium tubes were pushed into the sediment using the manipulator arm of the ROV (Fig. 1). Upon recovery, the cores were transferred to polycarbonate sleeves and immediately frozen to minimize oxidation. Cores were collected from the active orifices of two vent sites (Vent 1 and Vent 2). Core YL17U01 was collected from the aperture of Vent 2 (Max. T = 144 °C) and YL17U02 was obtained from ~1 m away; core YL17U03 was obtained from the aperture of Vent 1 (Max. T = 174 °C) and YL17U04 was obtained from ~1 m away. The mineralogy and texture of the cores has been described previously (Fowler et al., 2019). Briefly, all of the cores are clast supported semi-lithified mud breccia pervasively altered predominantly to kaolinite (up to 90%), with boehmite, pyrite, and trace pyrrhotite.

Pyrite grains were obtained for analysis from the base of the two cores recovered from active vents, and the base and top of the two cores collected ~1 m from the vents. In addition, a thin (~0.5 mm wide) discontinuous pyrite "vein" was sampled from ~5 cm below the top of core YL17U02. A volume of sediment with dimensions of ~0.5 cm vertically × 0.5 cm deep × 2 cm horizontally was removed from the six sample intervals. Approximately 0.5 g of this material was utilized to determine pyrrhotite occurrence (see below). Pyrite separates for sulfur isotope analysis were concentrated from the sediment by sonic agitation in distilled water, decanting the supernatant to recover the coarse fraction, rinsing the coarse particles several times with deionized water, followed by air drying. The morphology of the pyrite grains was investigated using an SEM at the LaCORE facility at the University of Minnesota. Pyrite was hand-picked from the remainder of the coarse fraction and mounted in a 25 mm diameter epoxy disc together with grains of Sonora pyrite (Farquhar et al., 2013). The disc was polished to expose the interior of the pyrite grains and to create a surface with less than a few microns of relief, and was subsequently gold coated for SIMS analysis.

3.2. Analytical procedures and notation

Pyrrhotite occurrence was determined from hysteresis loops measured on a Princeton Instruments vibrating sample magnetometer and zero-field low temperature cycling

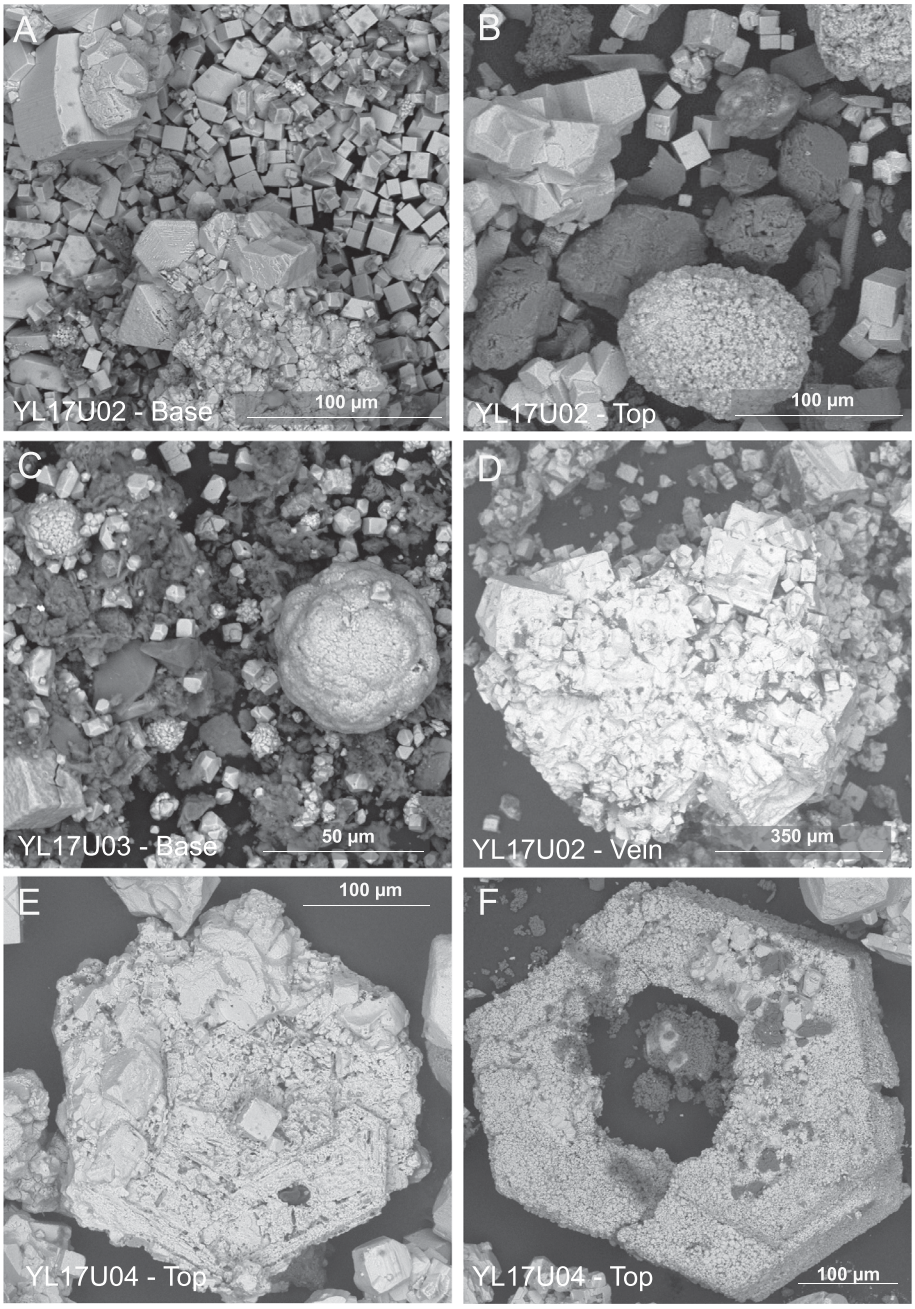

Fig. 3. A–F. SEM images of representative pyrite morphologies separated from sediments collected within and offset from active hydrothermal vents offshore of Stevenson Island in Yellowstone Lake. (A) Pyrite cubes present at the base of offset core YL17U02. (B) Framboidal pyrite and pyrite cubes present in the silt layer of core YL17U02 (material with darker backscatter is predominantly boehmite with some diatom fragments). (C) Framboidal pyrite and pyrite cubes present in kaolinite at the base of core YL17U03, which was collected from an active vent (material with darker backscatter is predominantly kaolinite and diatom fragments). (D) Pyrite vein consisting of aggregated pyrite cubes from core YL17U02, which was collected ~1 m from an active vent. E and (F) Pyrrhotite replaced by pyrite present in core YL17U04.

(300 K–10 K) of a room temperature saturating isothermal remanent magnetization (RTSIRM), acquired in a 2.5 T field on a Quantum Design Magnetic Property Measurement System (MPMS) at the Institute for Rock Magnetism at the University of Minnesota, USA. The cooling rate and step size was 5 K/min. The saturation magnetization (M_s) determined from hysteresis loop data after correction for paramagnetic contributions was used to qualitatively estimate the ferrimagnetic component in samples.

Sulfur isotope (^{32}S, ^{33}S, and ^{34}S) analyses were performed using a Cameca IMS 1280 SIMS at the Institute of Geology and Geophysics (Beijing), at the Chinese Academy of Sciences (Table 1). Spots were selected for analysis utilizing back scattered electron (BSE) images to avoid

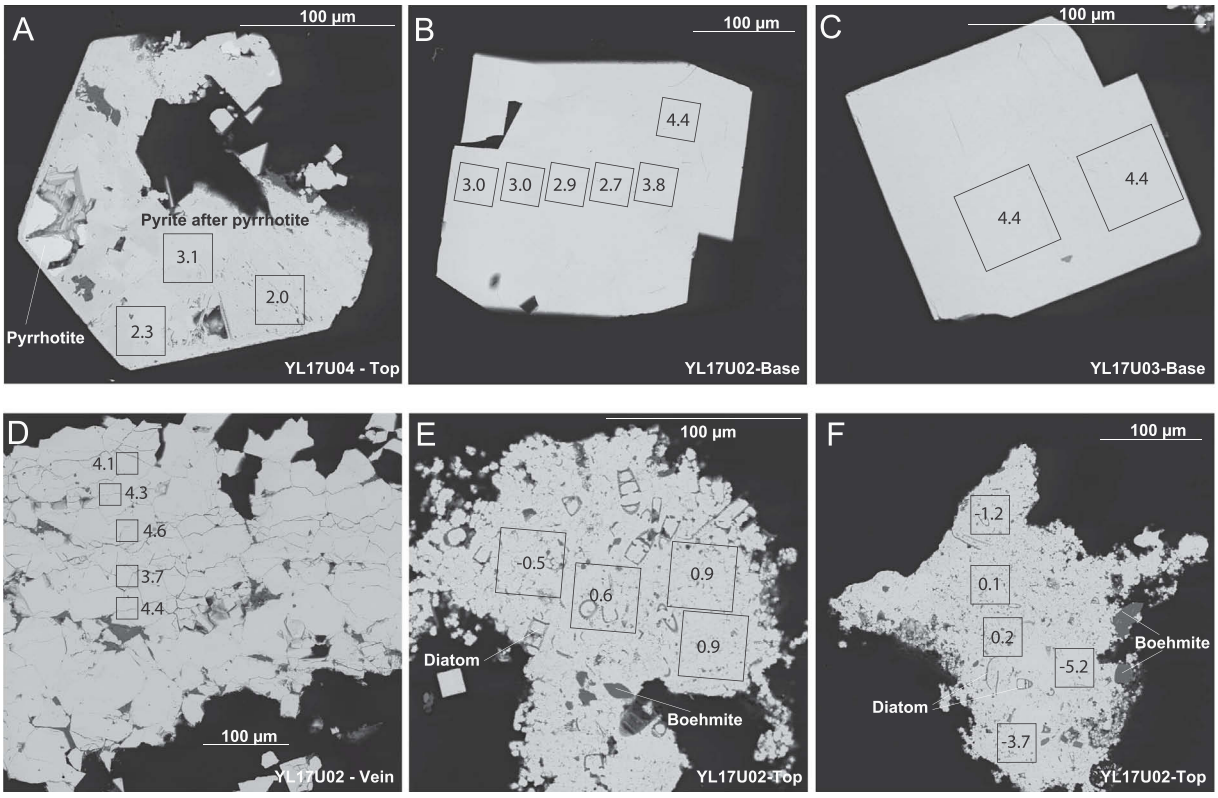

Fig. 4. A–F. Selected BSE images of analyzed pyrite, squares represent locations where SIMS data was acquired, numbers represent $\delta^{34}S$ measurements. (A) pyrrhotite largely replaced by pyrite from offset core YL17U04. (B) Cubic pyrite from the base of offset core YL17U02. (C) Cubic pyrite from the base of vent throat core YL17U03. (D) Pyrite vein from core YL17U02. (E) Framboidal and (F) pseudo framboidal pyrite from the top of offset core YL17U02.

defects and other phases. For the SIMS analysis, the Cs^+ primary ion beam was accelerated at 10 kV with an intensity of 1.8 to 2.3 nA. Each analysis was obtained using a 25×25 µm spot, which was produced from a ~15 µm diameter beam scanned over a 10×10 µm grid. An electron gun was not used to neutralize the possible buildup of positive charges since pyrite is a good conductor. Secondary ions were accelerated at 10 kV, and $^{32}S^-$, $^{33}S^-$, $^{34}S^-$ were detected simultaneously with three Faraday cups. A nuclear magnetic resonance regulator was used to stabilize the magnetic field. The intensity of $^{32}S^-$ was typically above 1.3×10^9 counts per second (cps), and the mass resolution was ~2400. A step-shaped peak was obtained with a ^{33}S peak on the left and a $^{32}S^1H$ peak on the right. To avoid interference from $^{32}S^1H^-$, the magnetic field strength was tuned to measure the flat portion on the left side of the $^{33}S^-$ peak (e.g. Chen et al., 2015). Each analysis took about 4.5 min, including pre-sputtering (30 s), automated centering of the secondary ions (60 s), and integration of the sulfur isotope signals (160 s; 40 cycles × 4 s).

Sonora pyrite was used as a running standard and was analyzed twice after every 8 samples. Measured isotope ratios were converted to delta notation by normalizing to Vienna Canyon Diablo Troilite (VCDT), using values obtained from Ding et al. (2001) ($^{34}S/^{32}S = 0.044163$, $^{33}S/^{32}S = 0.007877$). The Sonora pyrite standard ($\delta^{34}S_{VCDT} = 1.61‰$ and $\delta^{33}S_{VCDT} = 0.83‰$; (Farquhar et al., 2013)) was measured to correct for instrument mass fractionation. The external reproducibility of $\delta^{34}S_{VCDT}$ and $\delta^{33}S_{VCDT}$ based on 40 Sonora pyrite measurements was 0.16‰ and 0.10‰, respectively, which was propagated into the uncertainties of the unknowns. Additional details regarding the analytical and standardization method are provided by Chen et al. (2015).

Sulfur isotope values are reported using standard delta notation (Table 1), which is suited for illustrating linear relationships during mixing processes (Ono et al., 2007; Rouxel et al., 2008):

$$\delta^x S = ({}^x R_{sample} / {}^x R_{VCDT} - 1) \times 1000 \quad (6)$$

where $^xR_{sample}$ and $^xR_{VCDT}$ are the isotope ratios of the sample and VCDT, respectively (x = 33 or 34). The standard definition for $\Delta^{33}S$ is used:

$$\Delta^{33} S = {}^{33} S - 0.515 \times \delta^{34} S \quad (7)$$

4. RESULTS

A drop in magnetization at ≈ 30 kelvin in the RTSIRM data (Fig. 2) is typical for the Besnus transition in monoclinic pyrrhotite (Besnus and Meyer, 1964; Volk et al., 2018). The samples have a large paramagnetic component, visible as a linear positive slope at high magnetic fields in the hysteresis loops. Assuming no other ferrimagnetic

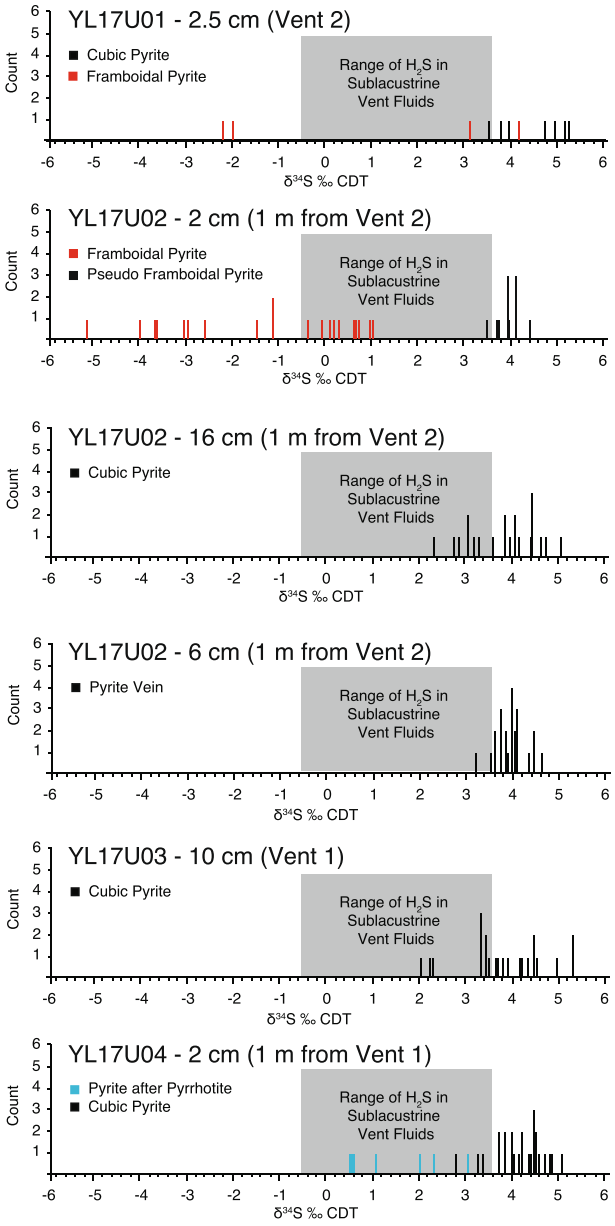

Fig. 5. $\delta^{34}S$ of pyrite in sediment cores form sublacustrine hydrothermal vents in Yellowstone Lake. Framboidal pyrite span a range of $\delta^{34}S$ values from those of H_2S in vent fluids to several ‰ lower, indicative of biological sulfate reduction at temperature conditions well below the maximum measured temperatures of 174 °C and 144 °C for Vent 1 and Vent 2 fluids, respectively. Cubic pyrite and pyrrhotite with $\delta^{34}S$ values in the range of H_2S from vent fluids are interpreted to form by the H_2S pathway in low-pH fluids and at reducing conditions compatible with low ratios of lake water/vent fluid mixing. Cubic pyrite with $\delta^{34}S$ values that range up to several ‰ heavier than H_2S in vent fluids are interpreted to form by the polysulfide pathway in near neutral and more oxidized fluids at higher lake water/vent fluid mixing ratios. That these pyrite forms coexist in discrete sediment samples suggests the redox front at these vents is transient with time. Values for $\delta^{34}S$ of H_2S in vent fluids are from throughout the lake (Gemery-Hill et al. (2007).

minerals are present in the samples, the amount of monoclinic pyrrhotite can be determined by relating M_s of the sample with that of pyrrhotite. However, some samples showed signs of different magnetic mineral, magnetite, for example YL17U03 – 2 cm, which shows signs of the magnetite Verwey transition (≈120 K) in the RTSIRM data. Thus, estimates for pyrrhotite content are a maximum for the monoclinic pyrrhotite variety, and accounts for <0.5 weight percent in samples when present.

The following pyrite morphologies were identified: disseminated cubic pyrite grains, framboidal pyrite, veins of aggregated cubic pyrite, and pyrrhotite replaced by pyrite (Fig. 3). Cubic pyrite (<10 μm to ~ 50 μm) is the dominant morphology in all samples (Fig. 3A through 3D). Framboidal pyrite (<10 μm to 100 μm) and pseudo framboidal pyrite (i.e. aggregates of pyrite approximating a spherical form) are more common in cores 1 m from active vents (Fig. 3B) but also present in cores collected from active vents (Fig. 3C). Several thin (~1 mm wide) and discontinuous (<50 mm long) veins of aggregated cubic pyrite occur in the clay immediately below a 5 cm-thick silt cap that overlies breccia (Fowler et al., 2019) in offset core YL17U02 (Fig. 3D). Pyrrhotite replaced by pyrite occurs in all cores and can be distinguished based on the hexagonal form (Fig. 3E and F).

There are no obvious growth zones in the analyzed pyrite as observed in BSE images, although impurities and defects are present to different degrees. Samples of pyrite replacing pyrrhotite contain voids formed between growing crystals, and remnants of the $Fe_{(1-X)}S$ precursor that are apparent from the brighter back scatter in BSE images (Fig. 4A). Pyrite cubes are homogenous and have no obvious inclusions (Fig. 4B & C). The pyrite vein from core YL17U02 also has no obvious zoning or inclusions, and forms neat pyrite cubes when fractured (Fig. 4D). Framboidal pyrite (Fig. 4E) and pseudo framboids (Fig. 4F) are composed of <5 μm pyrite microlites that encompass boehmite and pyritized diatoms inclusions.

Sulfur isotope values are distinct and vary according to the morphology of pyrite. Two pyritized pyrrhotite grains were analyzed, and $\delta^{34}S$ values range from +0.5 to +3.1‰ (average 1.6‰) for n = 6 total analyses (Fig. 5A). Intragrain $\delta^{34}S$ variations were +0.5 and +1.1‰ for the two analyzed grains, respectively. Forty different grains of cubic pyrite from the four cores were analyzed; multiple spots including the core and rim were analyzed on 17 of these grains. In addition, 5 transects consisting of 4 or 5 spot analyses were measured across the pyrite vein from core YL17U02. The $\delta^{34}S$ values for all (n = 96) inter- and intragrain analyses of cubic and vein pyrite range from +2.0 to +5.3‰ (average 4.0‰) (Fig. 5A and B). Intragrain $\delta^{34}S$ variations ranged from 0 to +1.9‰ for the cubic pyrite, and by +1.4‰ for the vein pyrite. The range of reported $\delta^{34}S$ variations exceed the 3σ value of 0.24‰ for 25 replicate analyses of the Sonora pyrite standard, thus, are statistically significant. The $\Delta^{33}S$ values for pyrite replacing pyrrhotite, cubic pyrite, and vein pyrite are within analytical precision of 0.11‰ (3 σvalue for 25 replicates of the Sonora pyrite standard), thus, are not reported.

Nine different framboidal and pseudo-framboidal pyrites were measured and transects of individual spot analyses were completed on five of these grains. Two pseudo pyrite

framboids were analyzed with transects of four and six spot analyses, respectively. The $\delta^{34}S$ values of framboidal and pseudo framboidal pyrite range from –5.2 to +4.3‰ (average +0.6‰) and $\Delta^{33}S$ values range from +0.10 to +0.30‰ (average 0.20‰) for n = 32 total analyses (Fig. 5C). Intragrain $\delta^{34}S$ variations in framboidal and pseudo framboidal pyrite ranged from +0.4 to +5.4‰ and intragrain $\Delta^{33}S$ varied by +0.4 to +0.14‰.

5. DISCUSSION

5.1. The source and cycling of sulfur in subaerial Yellowstone thermal springs

H_2S and H_2S- derived aqueous sulfide species in subaerial Yellowstone fumaroles and hot springs fall in a narrow range of $\delta^{34}S$ values between −1.2 and +2.6‰ (Schoen and Rye, 1970; Bergfeld et al., 2014; Kamyshny et al., 2014). Sulfur isotope values of dissolved sulfide in Yellowstone Lake sublacustrine hydrothermal vent waters fall in a similar range ($\delta^{34}S = -0.5$ to +3.6‰) as subaerial hot springs (Shanks et al., 2007). These sulfur isotope values correspond to a mantle sulfur source that is mobilized through the reaction of meteoric fluids with mantle-derived basalts and possible contributions from magmatic gases (Lowenstern et al., 2015). Mixing between subaerial Yellowstone geothermal fluids and oxygenated surface waters results in non-equilibrium sulfide oxidation to produce sulfate and sulfur species with intermediate oxidation states between sulfide and sulfate (Truesdell, 1991; Xu et al., 2000) that can be enriched in $\delta^{34}S$ by several per mil (Kamyshny et al., 2014). Intermediate sulfur species detected in Deep Hole sublacustrine vent fluids (e.g. Yang et al., 2011) suggests rapid non-equilibrium sulfide oxidation similarly occurs at sublacustrine hydrothermal mixing interfaces in Yellowstone Lake. Sulfur cycling in many subaerial Yellowstone geothermal springs is influenced by both abiotic sulfide oxidation and microbial sulfate reduction processes (Fishbain et al., 2003; Roychoudhury, 2004; Spear et al., 2005; Kamyshny et al., 2014), processes also implicated at Deep Hole sublacustrine vents by the present study.

5.2. Sublacustrine sulfur cycling recorded by sulfur isotope measurements of pyrite in Deep Hole hydrothermal sediments

5.2.1. Pyritized pyrrhotite

Well crystalized pyrrhotite commonly forms in subsurface geothermal steam zones where high concentrations of H_2 and H_2S provide sufficiently reducing conditions at temperatures that exceed the threshold for microbial activity (Steiner and Rafter, 1966; Browne and Ellis, 1970; Hedenquist, 1990; Simmons and Browne, 2000). The $\delta^{34}S$ of pyrrhotite formed in this environment often reflects that of the source sulfide (Steiner and Rafter, 1966), given the minimal fractionation between pyrrhotite and the sulfide from which it forms (Ohmoto and Rye, 1979). Monoclinic pyrrhotite replaced by pyrite in ore-forming systems has been interpreted to indicate a shift in temperature or redox conditions, which destabilizes pyrrhotite, while providing requisite $FeS_{(s)}$ for pyrite growth (Qian et al., 2011 and references therein). That monoclinic pyrrhotite is unstable in the current vent system is apparent from its overgrowth and replacement by pyrite, and the partial dissolution of some pyrrhotite grains (Figs. 3E, F, and 4A).

Pyrite formed through the H_2S pathway has an isotopic composition intermediate to that of the $FeS_{(aq)}$ and H_2S reservoirs, as it contains stoichiometrically equivalent proportions of sulfur from both sources (Butler et al., 2004). That the $\delta^{34}S$ values of the pyrite replacing pyrrhotite (+0.5 to +3.1‰) fall within the range of $H_2S_{(aq)}$ in Yellowstone Lake sublacustrine vent fluids (−0.5 to +3.6‰) reported by Gemery-Hill et al. (2007) (Fig. 5), suggests that both the $FeS_{(aq)}$ and sulfur species involved in sulfidation of $FeS_{(aq)}$ had near-mantle $\delta^{34}S$ values. The indistinguishable $\delta^{34}S$ values of the pyrite replacing pyrrhotite (Fig. 5) is consistent with abiotic formation. However, statistically significant intragrain $\delta^{34}S$ variations of over 1‰ in pyrite replacing pyrrhotite suggests contributions from a sulfur reservoir with a fluctuating $\delta^{34}S$ composition. As opposed to pyrite formed via the H_2S pathway, the intragrain $\delta^{34}S$ variations may reflect variable $FeS_{(aq)}$ sulfidation by an intermediate sulfur species with $\delta^{34}S$ values affected by an irreversible abiotic oxidative process.

5.2.2. Cubic and vein pyrite

The $\delta^{34}S$ values of cubic and vein pyrite (+2.0 to +5.3‰) extend from the range of mantle sulfide to at least +1.7‰ heavier than dissolved sulfide in vent fluids (e.g. $\delta^{34}S = -0.5$ to +3.6‰; Shanks et al., 2007), indicating sulfur contributions from an isotopically heavy sulfur reservoir. Intragrain $\delta^{34}S$ variations of up to +1.9‰ for individual pyrite cubes further suggest transient availability of this heavy sulfur reservoir. It is noteworthy that the magnitude of isotopic variation reflected by cubic and vein pyrite is equivalent to that observed between dissolved sulfide and the more oxidized sulfur species produced in subaerial Yellowstone hotsprings, a fractionation attributed to sulfur isotope disequilibrium by sulfide oxidation (e.g. Kamyshny et al., 2014). The inherently unstable nature of a sublacustrine steam condensation interface, which migrates vertically following pressure changes from lake level fluctuations or source temperature changes, may influence extent of oxidative mixing at a given locus (Schubert et al., 1980; Fowler et al., 2019).

Polysulfides can constitute a significant proportion of sulfur in a system above about pH 6 and temperatures below 200 °C (Chen and Morris, 1972; Giggenbach, 1974; Berndt et al., 1994; Kamyshny et al., 2004; Kamyshny et al., 2006). Polysulfide species are stable in neutral to alkaline solutions, therefore the rate of pyrite formed via the polysulfide pathway increases with increasing pH (Rickard and Luther, 2007). Thus, the polysulfide pathway may be important for abiotic pyrite formation in transitional pH and redox environments (Rickard, 1997). The isotopic composition of pyrite formed by the polysulfide pathway (Eq. (2)) is dominated by the isotopic composition of the polysulfide reservoir, as the reaction mechanism involves sulfur exchange between $FeS_{(aq)}$ and polysulfide (Butler et al., 2004; Hunger and Benning, 2007). At ambient

temperature, polysulfides can be enriched in $\delta^{34}S$ by up to 4‰ compared to the initial sulfide source, with the extent of fractionation increasing as a function of polysulfide chain length (Amrani et al., 2006). At more elevated temperatures, sulfide oxidation has been shown to produce intermediate sulfur species enriched in $\delta^{34}S$ by up to 2‰, as verified in samples from pH > 4 and up to 93 °C YNP geothermal pools (Kamyshny et al., 2014).

A determinant factor in pyrite formation by the polysulfide pathway is the rate at which reduced sulfur is oxidized. While H_2S in subaqueous hydrothermal vent fluids is oxidized to intermediate sulfur species and ultimately sulfate by mixing with oxygenated bottom waters, the reaction of sulfide with oxygen is unfavorable despite a negative delta-G because of activation energy constraints (Luther and Ferdelman, 1993) and is always kinetically slow (Chen and Morris, 1972; Millero et al., 1987). In contrast, laboratory experiments have demonstrated abiotic polysulfide formation in <10 seconds at ambient temperatures in sulfur undersaturated solutions (Kamyshny et al., 2003), albeit formation is slower in sulfur-saturated solutions (Kafantaris, 2017; Avetisyan et al., 2019). Whilst oxidation limits polysulfides to relatively low levels at low concentrations particularly at pH values as low as 4 (Kamyshny et al., 2003; Kamyshny et al., 2014), the rapid reactivity of polysulfide provides a small but constantly replenished reservoir if an elemental sulfur and sulfide supply is maintained. Furthermore, voltammetry studies have shown that abundant polysulfide concentrations occur at *in situ* at pH values as low 6–6.8 at hydrothermal vent mixing zones in the presence of trace Fe^{2+} (Rozan et al., 2000; Luther et al., 2001; Gartman et al., 2011). In this situation, rapid kinetics of Fe^{2+} oxidation by O_2 produces sufficient Fe^{3+}, which facilitates the transformation of H_2S to polysulfides in seconds (Vazquez et al., 1989; Luther et al., 2001).

While sulfide oxidation and polysulfide production is attributed to abiotic processes in subaerial Yellowstone springs (Kamyshny et al., 2014), both sulfide oxidizing and sulfate reducing organisms have been identified in and around hydrothermal vents in Yellowstone Lake (Klump et al., 1988; Yang et al., 2011; Inskeep et al., 2015; Kan et al., 2016). Considering that many microbial sulfide oxidation processes may produce similar $\delta^{34}S$ variations to abiotic processes (Toran and Harris, 1989), it is difficult to resolve unambiguously the relative role of abiotic or microbial processes in the sublacustrine vents. Clearly, biologic sulfide oxidation would not be possible at the *in situ* temperatures of liquid vent fluids where the vent aperture sediment cores were recovered (maximum of 174 °C; Tan et al., 2017). Therefore, interpreting formation of the cubic pyrite samples as a biological sulfide oxidation process would require further temporal change in the location or temperature of hydrothermal venting. We suggest that the $\delta^{34}S$-enriched values of cubic and vein pyrite reflect sulfur contributions from $\delta^{34}S$-enriched polysulfide produced from $H_2S_{(aq)}$ oxidation at a higher mixing ratio between lake water and steam condensate, where pH and Eh would be elevated. The occurrence of elevated Fe in Yellowstone Lake hydrothermal vent waters (Gemery-Hill et al., 2007) provides a mechanism to catalyze abiotic polysulfide formation.

5.2.3. Framboidal and pseudo-framboidal pyrite

Depleted $\delta^{34}S$ and elevated $\Delta^{33}S$ values are distinct indicators of biologic sulfate reduction (Canfield, 2001; Ono et al., 2006; Ono et al., 2012). Intermediate sulfur species incorporated into pyrite can be produced by microbial reduction of sulfate by H_2 consuming microbes, a process characterized by modest $\delta^{34}S$ depletions of −5 to −10‰ relative to the starting sulfate (Kaplan and Rittenberg, 1964; Canfield et al., 1998). The $\delta^{34}S$ values of the framboidal and pseudo framboidal pyrite in the present study (–5.2 to +4.3‰) are notably within this range of depletion relative to SO_4^{2-} ($\delta^{34}S_{SO4} = 1.7$ to 4.6‰, averaging 2.5‰) reported for Yellowstone Lake (Gemery-Hill et al., 2007; Shanks et al., 2007), and consistent with H_2 consuming microbes previously identified at Deep Hole vents (Yang et al., 2011). Elevated $\Delta^{33}S$ values of +0.1 to +0.3‰ for the framboidal pyrite are significant within the range of analytical precision for the SIMS measurements reported here and are similarly consistent with processes typical of microbial sulfate reduction (Ono et al., 2006; Ono et al., 2007; Ono et al., 2012).

Considering the extremely low concentration of sulfate in Yellowstone Lake water (0.11 mmol/kg; Fowler et al., 2019), it is reasonable to assume that microbial sulfate reduction could exceed the sulfate supply of lake water mixing into the low-permeability kaolinitic sediments that host the vents. Therefore, we assess microbial sulfate reduction using a simple closed system equilibrium model (Ono et al., 2007) in $\delta^{34}S$ and $\Delta^{33}S$ space following the procedure of Ono et al. (2006) (Fig. 6). While equilibrium is almost

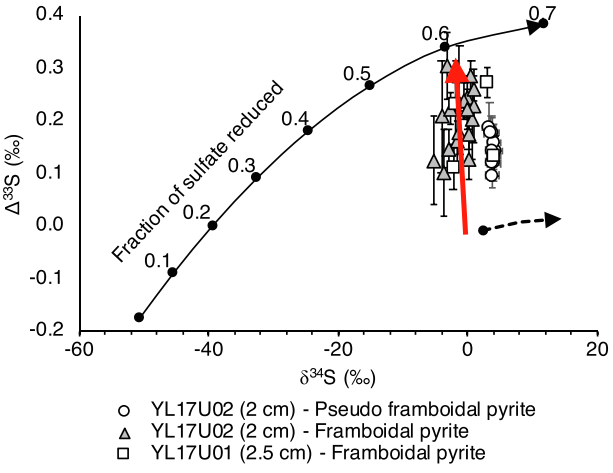

Fig. 6. Closed system sulfate reduction model, after (Ono et al., 2006), expressed in delta notation (see text for details). Framboidal pyrite falls on a mixing line (red arrow) between mantle sulfide and a ~60% reduction of lake water sulfate with an average $\delta^{34}S = 2.5$‰ and $\Delta^{33}S = 0$‰. Vertical error bars are the standard error of pyrite $\Delta^{33}S$. Horizontal error bars are the standard error of $\delta^{34}S$ measurements, which are smaller than the symbols utilized. The dashed arrow shows the evolution of the remaining lake water sulfate.

certainly not attained for the conditions at and around Deep Hole hydrothermal vents, the application provides a framework to interpret a more complex disequilibrium system. Results suggest that $\Delta^{33}S$ values of framboidal and pseudo-framboidal pyrite could be attributed to ~60% reduction of lake water sulfate. The variability in $\delta^{34}S$ values may be attributed to a range of processes that include sulfur recycling and mixing within microbial communities (e.g. Canfield and Teske, 1996), while variations in $\Delta^{33}S$ may be attributed to a combination of mixing with mantle sulfide and limitations in equilibrium assumptions or analytical resolution. Regardless, the $\delta^{34}S$ and mass independent $\Delta^{33}S$ fractionations are clearly characteristic of microbial sulfate reduction that could not occur at the active *in situ* temperature conditions, implying a change in temperature above the threshold for microbial activity, or transience in the venting location with time.

6. CONCLUSIONS

Hydrothermal fluids issuing from altered sediments on the floor of Yellowstone Lake reveal complex patterns of sulfide mineralization with distinct sulfur isotope compositions, broadly consistent with the characteristics of subsurface geothermal steam dominated systems elsewhere (Browne and Ellis, 1970; Hedenquist, 1990; Cox and Browne, 1995; Simmons and Browne, 2000). In Yellowstone Lake sediments, sulfide mineralization is localized where slightly acidic, reducing and hot steam condensate mixes with neutral pH, cold and oxidizing lake water. Pyrrhotite, confirmed by magnetic techniques, occurs at the most reducing conditions associated with this redox front. Sulfide oxidation across the redox front has produced pyrite by the following mechanisms: (1) addition to $FeS_{(aq)}$ of an intermediate sulfur species, probably polysulfide, formed through disequilibrium oxidation of magmatic $H_2S_{(aq)}$; and (2) dissimilatory reduction of sulfate by microbes to produce products for pyrite formation.

The co-occurrence of pyrite formed by distinct processes and notable intragrain sulfur isotope variations observed using micro analytical techniques suggest dynamic redox conditions at individual vents over time. SEM images of partially dissolved pyrrhotite crystals replaced by pyrite reveal a shift to more oxidizing conditions. The sulfur isotope composition of the replacement pyrite is largely indistinguishable from the mantle sulfide in vent fluids, although variable intragrain $\delta^{34}S$ values implicate the formation of intermediate valence sulfur species with associated sulfur isotope fractionations. The occurrence of cubic and vein pyrite with $\delta^{34}S$ values several per mil heavier than mantle sulfide suggests a stage where oxidation was sufficient to produce polysulfide species with distinctive $\delta^{34}S$ fractionations. Importantly, the $\delta^{34}S$ values within individual cubic pyrite crystals are heterogeneous to the extent observed by SIMS data and suggest fluctuating redox conditions that periodically produced polysulfide species with variable chain lengths and corresponding $\delta^{34}S$ fractionations. Framboidal pyrite with $\delta^{34}S$ several per mil lighter than H_2S in vent fluids is interpreted to have formed from microbial sulfate reduction, and implies a stage where the temperature was sufficiently low to support microbial activity.

The external cause for evolving conditions is not clear, but could involve fluctuations in lake level, changes in steam condensate flux, or spatial changes in sediment physical/chemical properties owing to sediment reactivity or variations in the fluid flow path. The role of these factors in Deep Hole vent formation is an active area of study (Sohn et al., 2017) that is beyond the goal of the present study. The sulfur isotope data and interpretations in the present work, however, suggest that the locus of venting in the Deep Hole is dynamic and has fluctuated in temperature and shifted in space through time.

ACKNOWLEDGEMENT, SAMPLES, AND DATA

This work was funded by the National Key R&D Program of China (2016YFE0203000) and NSF grants EAR 1515377 and OCE 1434798. The authors thank Dave Lovalvo, Todd Gregory, Bobby Mohr, and Josh Carlson from the Global Foundation for Ocean Exploration for their efforts in obtaining core materials utilized in this study. We thank Yang Li, Yu Liu, Guoqiang Tang for their help during the SIMS analyses. We also thank Dr. Rob Sohn and members of the HD-YLAKE research team for constructive advice. Part of this work was performed at the Institute for Rock Magnetism (IRM) at the University of Minnesota. The IRM is a U.S. National Multi-user Facility supported through the Instrumentation and Facilities program of the National Science Foundation, Earth Sciences Division, and by funding from the University of Minnesota. All work in Yellowstone National Park was completed under an authorized Yellowstone Research permit (YELL-2018-SCI-7018.

APPENDIX A. SUPPLEMENTARY MATERIAL

Supplementary data to this article can be found online at https://doi.org/10.1016/j.gca.2019.09.004.

REFERENCES

Amrani A., Kamyshny, Jr., A., Ovadia L. and Aizenshtat Z. (2006) Sulfur stable isotope distribution of polysulfide anions in an $(NH_4)_2Sn$ aqueous solution. *Inorg. Chem.* **45**, 1427–1429.

Avetisyan K., Buchshtav T. and Kamyshny A. (2019) Kinetics and mechanism of polysulfides formation by a reaction between hydrogen sulfide and orthorhombic cyclooctasulfur. *Geochim. Cosmochim. Acta* **247**, 96–105.

Bergfeld D., Lowenstern J. B., Hunt A. G., Shanks, III, W. C. and Evans W. (2014) Gas and isotope chemistry of thermal features in Yellowstone National Park, Wyoming (ver. 1.1, September 2014). In *US Geological Survey Scientific Investigations Report 2011-5012*, p. 28.

Berndt M. E., Buttram T., Early, III, D. and Seyfried, Jr, W. E. (1994) The stability of gold polysulfide complexes in aqueous sulfide solutions- 100 to 150°C and 100 bars. *Geochim. Cosmochim. Acta* **58**, 587–594.

Berner R. A. (1970) Sedimentary pyrite formation. *Am. J. Sci.* **268**, 1–23.

Berner R. A. (1983) Sedimentary pyrite formation: An update. *Geochim. Cosmochim. Acta* **48**, 605–615.

Besnus M. J. and Meyer A. J. (1964) Nouvelles données expérimentales sur le magnétisme de la pyrrhotine naturelle. In *Proceedings of the International Conference on Magnetism*, vol.

20, pp. 507–511. Proceedings of the International Conference on Magnetism.

Browne P. R. L. and Ellis A. J. (1970) The Ohaki-Broadlands hydrothermal area, New Zealand: Mineralogy and related geochemistry. *Am. J. Sci.* **269**, 97–131.

Butler I. B., Böttcher M. E., Rickard D. and Oldroyd A. (2004) Sulfur isotope partitioning during experimental formation of pyrite via the polysulfide and hydrogen sulfide pathways: implications for the interpretation of sedimentary and hydrothermal pyrite isotope records. *Earth Planet. Sci. Lett.* **228**, 495–509.

Canfield D. E. (2001) Biogeochemistry of sulfur isotopes. *Rev. Mineral. Geochem.* **43**, 607–636.

Canfield D. E. and Teske A. (1996) Late Proterozoic rise in atmospheric oxygen concentration inferred from phylogenetic and sulphur-isotope studies. *Nature* **382**, 127–132.

Canfield D. E. and Thamdrup B. (1994) The production of 34S-depleted sulfide during bacterial disproportionation of elemental sulfur. *Science* **266**, 1973–1975.

Canfield D. E., Thamdrup B. and Fleischer S. (1998) Isotope fractionation and sulfur metabolism by pure and enrichment cultures of elemental sulfur-disproportionating bacteria. *Limnol. Oceanogr.* **43**, 253–264.

Chen K. Y. and Morris J. C. (1972) Kinetics of oxidation of aqueous sulfide by oxygen. *Environ. Sci. Technol.* **6**, 529–537.

Chen L., Li X.-H., Li J.-W., Hofstra A. H., Liu Y. and Koenig A. E. (2015) Extreme variation of sulfur isotopic compositions in pyrite from the Qiuling sediment-hosted gold deposit, West Qinling orogen, central China: an in situ SIMS study with implications for the source of sulfur. *Miner. Deposita* **50**, 643–656.

Cox M. E. and Browne P. R. L. (1995) The occurrence of pyrrhotite in the Ngawha geothermal system, New Zealand. In *Proceedings of the 17th New Zealand Geothermal Workshop*, pp. 35–40.

Ding T., Valkiers S., Kipphardt H., De Bievre P., Taylor P. D. P., Gonfiantini R. and Krouse R. (2001) Calibrated sulfur isotope abundance ratios of three IAEA sulfur isotope reference materials and V-CDT with a reassessment of the atomic weight of sulfur. *Geochim. Cosmochim. Acta* **65**, 2433–2437.

Farquhar J., Cliff J., Zerkle A. L., Kamyshny, Jr., A., Poulton S. W., Claire M., Adams D. and Harms B. (2013) Pathways for Neoarchean pyrite formation constrained by mass-independent sulfur isotopes. *Proc. Natl. Acad. Sci. USA* **110**, 17638–17643.

Farquhar J., Johnston D. T., Wing B. A., Habicht K. S., Canfield D. E., Airieau S. and Thiemens M. H. (2003) Multiple sulphur isotopic interpretations of biosynthetic pathways: implications for biological signatures in the sulphur isotope record. *Geobiology* **1**, 27–36.

Fishbain S., Dillon J. G., Gough H. L. and Stahl D. A. (2003) Linkage of high rates of sulfate reduction in Yellowstone hot springs to unique sequence types in the dissimilatory sulfate respiration pathway. *Appl. Environ. Microbiol.* **69**, 3663–3667.

Fowler A. P. G., Tan C., Cino C. D., Scheuermann P., Volk M. W. R., Shanks, III, W. C. and Seyfried, Jr., W. E. (2019) Vapor-driven sublacustrine vents in Yellowstone Lake, Wyoming. *Geology* **47**, 223–226.

Gartman A., Yücel M., Madison A. S., Chu D. W., Ma S., Janzen C. P., Becker E. L., Beinart R. A., Girguis P. R. and Luther, III, G. W. (2011) Sulfide oxidation across diffuse flow zones of hydrothermal vents. *Aquat. Geochem.* **17**, 583–601.

Gemery-Hill P. A., Shanks, III, W. C., Balistrieri L. S. and Lee G. K. (2007) Geochemical data for selected rivers, lake waters, hydrothermal vents, and subaerial geysers in Yellowstone National Park, Wyoming and vicinity, 1996–2004. In *In the Greater Yellowstone Area—Volcanic, Tectonic, and Hydrothermal Processes in the Yellowstone Geoecosystem. U.S. Geological Survey Professional Paper 1717*, pp. 365–426.

Giggenbach W. F. (1974) Equilibria involving polysulfide ions in aqueous sulfide solutions up to 240°. *Inorg. Chem.* **13**, 1724–1730.

Hedenquist J. W. (1990) The thermal and geochemical structure of the Broadlands-Ohaaki geothermal system, New Zealand. *Geothermics* **19**, 151–185.

Hunger S. and Benning L. G. (2007) Greigite: a true intermediate on the polysulfide pathway to pyrite. *Geochem. Trans.* **8**, 1.

Inskeep W. P., Jay Z. J., Macur R. E., Clingenpeel S., Tenney A., Lovalvo D., Beam J. P., Kozubal M. A., Shanks, III, W. C., Morgan L. A., Kan J., Gorby Y., Yooseph S. and Nealson K. (2015) Geomicrobiology of sublacustrine thermal vents in Yellowstone Lake: geochemical controls on microbial community structure and function. *Front. Microbiol.* **6**, 1044.

Jørgensen B. B. (1990) A thiosulfate shunt in the sulfur cycle of marine sediments. *Science* **249**, 152–154.

Jørgensen B. B., Zawacki L. X. and Jannasch H. W. (1990) Thermophilic bacterial sulfate reduction in deep-sea sediments at the Guaymas Basin hydrothermal vent site (Gulf of California). *Deep Sea Res.* **37**, 695–710.

Kafantaris F. C. (2017) *On the reactivity of nanoparticulate elemental sulfur: experimentation and field observations*. Ph.D. Thesis in the Department of Earth Sciences, Indiana University, p. 233.

Kamyshny, Jr., A., Druschel G., Mansaray Z. F. and Farquhar J. (2014) Multiple sulfur isotopes fractionations associated with abiotic sulfur transformations in Yellowstone National Park geothermal springs. *Geochem. Trans.* **15**, 7.

Kamyshny, Jr., A., Ekeltchik I., Gun J. and Lev O. (2006) Method for the determination of inorganic polysulfide distribution in aquatic systems. *Anal. Chem.* **78**, 2631–2639.

Kamyshny, Jr., A., Goifman A., Gun J., Rizkov D. and Lev O. (2004) Equilibrium distribution of polysulfide ions in aqueous solutions at 25 °C: A new approach for the study of polysulfides' equilibria. *Environ. Sci. Technol.* **38**, 6633–6644.

Kamyshny, Jr., A., Goifman A., Rizkov D. and Lev O. (2003) Kinetics of disproportionation of inorganic polysulfides in undersaturated aqueous solutions at environmentally relevant conditions. *Aquat. Geochem.* **9**, 291–304.

Kan J., Clingenpeel S., Dow C. L., McDermott T. R., Macur R. E., Inskeep W. P. and Nealson K. H. (2016) Geochemistry and mixing drive the spatial distribution of free-living Archaea and bacteria in Yellowstone Lake. *Front Microbiol* **7**, 210.

Kaplan I. R. and Rittenberg S. C. (1964) Microbiological fractionation of sulphur isotopes. *J. Gen. Microbiol.* **34**, 195–212.

Klump J. V., Remsen C. C. and Kaster J. L. (1988) The presence and potential impact of geothermal activity on the chemistry and biology of Yellowstone Lake, Wyoming. In *In Global Venting, Midwater and Benthic Ecological Processes. National Oceanic and Atmospheric Administration National Undersea Research Program Research Report no. 88-4* (eds. M. DeLuca and I. Babb), pp. 81–98.

Lowenstern J. B., Bergfeld D., Evans W. C. and Hunt A. G. (2015) Origins of geothermal gases at Yellowstone. *J. Volcanol. Geoth. Res.* **302**, 87–101.

Luther, III, G. W. (1991) Pyrite synthesis via polysulfide compounds. *Geochim. Cosmochim. Acta* **55**, 2839–2849.

Luther, III, G. W. and Ferdelman T. G. (1993) Voltammetric characterization of iron(II) sulfide complexes in laboratory solutions and in marine waters and porewaters. *Environ. Sci. Technol.* **27**, 1154–1163.

Luther, III, G. W., Glazer B. T., Hohmann L., Popp J. I., Taillefert M., Rozan T. F., Brendel P. J., Theberge S. M. and Nuzzio D.

B. (2001) Sulfur speciation monitored in situ with solid state gold amalgam voltammetric microelectrodes: polysulfides as a special case in sediments, microbial mats and hydrothermal vent waters. *J. Environ. Monit.* **3**, 61–66.

McKibben M. A. and Riciputi L. R. (1997) *Sulfur Isotopes by Ion Microprobe, Applications of Microanalytical Techniques to Understanding Mineralizing Processes*. Society of Economic Geologists.

Millero F. J., Hubinger S., Fernandez M. and Garnett S. (1987) Oxidation of H2S in seawater as a function of temperature, pH, and ionic strength. *Environ. Sci. Technol.* **21**, 439–443.

Mojzsis S. J., Coath C. D., Greenwood J. P., McKeegan K. D. and Harrison T. M. (2003) Mass-independent isotope effects in Archean (2.5 to 3.8 Ga) sedimentary sulfides determined by ion microprobe analysis. *Geochim. Cosmochim. Acta* **67**, 1635–1658.

Ohmoto H. and Lasaga A. C. (1982) Kinetics of reactions between aqueous sulfates and sulfides in hydrothermal systems. *Geochim. Cosmochim. Acta* **46**, 1727–1745.

Ohmoto H. and Rye R. O. (1979) Isotopes of sulfur and carbon. In *Geochemistry of Hydrothermal Ore Deposits* (ed. H. L. Barnes). J Wiley and Sons, pp. 509–567.

Ono S., Keller N. S., Rouxel O. and Alt J. C. (2012) Sulfur-33 constraints on the origin of secondary pyrite in altered oceanic basement. *Geochim. Cosmochim. Acta* **87**, 323–340.

Ono S., Shanks, III, W. C., Rouxel O. J. and Rumble D. (2007) S-33 constraints on the seawater sulfate contribution in modern seafloor hydrothermal vent sulfides. *Geochim. Cosmochim. Acta* **71**, 1170–1182.

Ono S., Wing B., Johnston D., Farquhar J. and Rumble D. (2006) Mass-dependent fractionation of quadruple stable sulfur isotope system as a new tracer of sulfur biogeochemical cycles. *Geochim. Cosmochim. Acta* **70**, 2238–2252.

Qian G., Xia F., Brugger J., Skinner W. M., Bei J., Chen G. and Pring A. (2011) Replacement of pyrrhotite by pyrite and marcasite under hydrothermal conditions up to 220 C: An experimental study of reaction textures and mechanisms. *Am. Mineral.* **96**, 1878–1893.

Rickard D. (1995) Kinetics of FeS precipitation: Part 1. Competing reaction mechanisms. *Geochim. Cosmochim. Acta* **59**, 4367–4379.

Rickard D. (1997) Kinetics of pyrite formation by the H2S oxidation of iron (II) monosulfide in aqueous solutions between 25 and 125°C- The rate equation. *Geochim. Cosmochim. Acta* **61**, 115–134.

Rickard D. and Luther, III, G. W. (2007) Chemistry of iron sulfides. *Chem. Rev.* **107**, 514–562.

Rickard D. T. (1975) Kinetics and mechanism of pyrite formation at low temperatures. *Am. J. Sci.* **275**, 636–652.

Rouxel O., Ono S., Alt J., Rumble D. and Ludden J. (2008) Sulfur isotope evidence for microbial sulfate reduction in altered oceanic basalts at ODP Site 801. *Earth Planet. Sci. Lett.* **268**, 110–123.

Roychoudhury A. (2004) Sulfate respiration in extreme environments: a kinetic study. *Geomicrobiol. J.* **21**, 33–43.

Rozan T. F., Theberge S. M. and Luther, III, G. W. (2000) Quantifying elemental sulfur (S0), bisulfide (HS−) and polysulfides (Sx2−) using a voltammetric method. *Anal. Chim. Acta* **415**, 175–184.

Schieber J. (2002) Sedimentary pyrite- A window into the microbial past. *Geology* **30**, 531–534.

Schoen R. and Rye R. O. (1970) Sulfur isotope distribution in solfataras, Yellowstone National Park. *Science* **170**, 1082–1084.

Schoonen M. A. A. and Barnes H. L. (1991a) Mechanisms of pyrite and marcasite formation from solution- III. Hydrothermal processes. *Geochim. Cosmochim. Acta* **55**, 3491–3504.

Schoonen M. A. A. and Barnes H. L. (1991b) Reactions forming pyrite and marcasite from solution: II. Via FeS precursors below 100 °C. *Geochim. Cosmochim. Acta* **55**, 1505–1514.

Schubert G., Straus J. M. and Grant M. A. (1980) A problem posed by vapour dominated geothermal systems. *Nature* **287**, 423–425.

Shanks, III, W. C. (2001) Stable isotopes in seafloor hydrothermal systems. *Rev. Mineral. Geochem.* **43**, 469–525.

Shanks, III, W. C., Alt J. C. and Morgan L. A. (2007) Geochemistry of sublacustrine hydrothermal deposits in Yellowstone Lake—Hydrothermal reactions, stable-isotope systematics, sinter deposition, and spire formation. In *In the Greater Yellowstone Area—Volcanic, Tectonic, and Hydrothermal Processes in the Yellowstone Geoecosystem. U.S. Geological Survey Professional Paper 1717*, pp. 201–234.

Shanks, III, W. C., Bischoff J. L. and Rosenbaur R. J. (1981) Seawater sulfate reduction and sulfur isotope fractionation in basaltic systems: Interaction of seawater with fayalite and magnetite at 200-350C. *Geochim. Cosmochim. Acta* **45**, 1977–1995.

Shanks, III, W. C. and Seyfried, Jr., W. E. (1987) Stable isotope studies of vent fluids and chimney minerals, southern Juan de Fuca Ridge: Sodium metasomatism and seawater sulfate reduction. *J. Geophys. Res. Solid Earth* **92**, 11387–11399.

Simmons S. F. and Browne P. R. L. (2000) Hydrothermal minerals and precious metals in the Broadlands-Ohaaki geothermal system: implications for understanding low-sulfidation epithermal environments. *Econ. Geol.* **95**, 971–999.

Slack J. F., Shanks W. C., Ridley W. I., Dusel-Bacon C., DesOrmeau J. W., Ramezani J. and Fayek M. (2019) Extreme sulfur isotope fractionation in the late Devonian dry creek volcanogenic massive sulfide deposit, Central Alaska. *Chem. Geol.*.

Sohn R., Harris R., Linder C., Luttrell K., Lovalvo D., Morgan L., Seyfried, Jr., W. E. and Shanks, III, W. C. (2017) Exploring the restless floor of Yellowstone Lake. *Eos*, 98.

Spear J. R., Walker J. J., McCollom T. M. and Pace N. R. (2005) Hydrogen and bioenergetics in the Yellowstone geothermal ecosystem. *Proc. Natl. Acad. Sci. USA* **102**, 2555–2560.

Steiner A. and Rafter T. A. (1966) Sulfur isotopes in pyrite, pyrrhotite, alunite and anhydrite from steam wells in the Taupo volcanic zone, New Zealand. *Econ. Geol.* **61**, 1115–1129.

Sweeney R. E. and Kaplan I. R. (1973) Pyrite framboid formation: laboratory synthesis and marine sediments. *Econ. Geol.* **68**, 618–634.

Tan C., Cino C. D., Ding K. and Seyfried W. E. (2017) High temperature hydrothermal vent fluids in Yellowstone Lake: Observations and insights from in-situ pH and redox measurements. *J. Volcanol. Geoth. Res.* **343**, 263–270.

Toran L. and Harris R. F. (1989) Interpretation of sulfur and oxygen isotopes in biological and abiological sulfide oxidation. *Geochim. Cosmochim. Acta* **53**, 2341–2348.

Truesdell A. H. (1991) Origins of acid fluids in geothermal systems. *Geothermal Resourc. Council Trans.* **15**, 289–296.

Vazquez F., Zhang J.-Z. and Millero F. J. (1989) Effect of metals on the rate of the oxidation of H2S in seawater. *Geophys. Res. Lett.* **16**, 1363–1366.

Volk M. W. R., McCalla E., Voigt B., Manno M., Leighton C. and Feinberg J. M. (2018) Changes in physical properties of 4C pyrrhotite (Fe_7S_8) across the 32 K Besnus transition. *Am. Mineral.* **103**, 1674–1689.

Wilkin R. T. and Barnes H. L. (1996) Pyrite formation by reactions of iron monosulfides with dissolved inorganic and organic sulfur species. *Geochim. Cosmochim. Acta* **60**, 4167–4179.

Woodruff L. G. and Shanks, III, W. C. (1988) Sulfur isotope study of chimney minerals and vent fluids from 21°N, East Pacific

Rise: Hydrothermal sulfur sources and disequilibrium sulfate reduction. *J. Geophys. Res. Solid Earth* **93**, 4562–4572.

Xu Y., Schoonen M. A. A., Nordstrom D. K., Cunningham K. M. and Ball J. W. (2000) Sulfur geochemistry of hydrothermal waters in Yellowstone National Park, Wyoming, USA. II. Formation and decomposition of thiosulfate and polythionate in Cinder Pool. *J. Volcanol. Geoth. Res.* **97**, 407–423.

Yang T., Lyons S., Aguilar C., Cuhel R. and Teske A. (2011) Microbial communities and chemosynthesis in Yellowstone Lake sublacustrine hydrothermal vent waters. *Front. Microbiol.* **2**, 130.

Associate editor: Wolfgang Bach